Intermodel spread in Walker circulation responses linked to spread in moist stability and radiation responses

Margaret L Duffy[1,2] and Paul A O'Gorman[2]

[1]National Center for Atmospheric Research
[2]Department of Earth, Atmospheric and Planetary Sciences, Massachusetts Institute of Technology

December 11, 2022

Abstract

The response of the Pacific Walker circulation (WC) to long-term warming remains uncertain. Here, we diagnose contributions to the WC response in comprehensive and idealized general circulation model (GCM) simulations. We find that the spread in WC response is substantial across both the Coupled Model Intercomparison Project (CMIP6) and the Atmospheric Model Intercomparison Project (AMIP) models, implicating differences in atmospheric models in the spread in projected WC strength. Using a moist static energy (MSE) budget, we evaluate the contributions to changes in the WC strength related to changes in gross moist stability (GMS), horizontal MSE advection, radiation, and surface fluxes. We find that the multimodel mean WC weakening is mostly related to changes in GMS and radiation. Furthermore, the *spread* in WC response is related to the spread in GMS and radiation responses. The GMS response is potentially sensitive to parameterized convective entrainment which can affect lapse rates and the depth of convection. We thus investigate the role of entrainment in setting the GMS response by varying the entrainment rate in an idealized GCM. The idealized GCM is run with a simplified Betts-Miller convection scheme, modified to represent entrainment. The weakening of the WC with warming in the idealized GCM is dampened when higher entrainment rates are used. However, the spread in GMS responses due to differing entrainment rates is much smaller than the spread in GMS responses across CMIP6 models. Therefore, further work is needed to understand the large spread in GMS responses across CMIP6 and AMIP models.

Intermodel spread in Walker circulation responses linked to spread in moist stability and radiation responses

Margaret L. Duffy[1,2], **Paul A. O'Gorman**[2]

[1]National Center for Atmospheric Research, Boulder, CO
[2]Department of Earth, Atmospheric and Planetary Sciences, Massachusetts Institute of Technology, Cambridge, MA

Key Points:

- The atmosphere plays an important role in setting the large spread in the Walker circulation (WC) response to warming in coupled models
- Energetic analysis shows the WC response and its spread are strongly related to the responses of the gross moist stability and radiation
- The responses of the WC and GMS exhibit some sensitivity to convective entrainment in an idealized general circulation model

Corresponding author: Margaret L. Duffy, `mlduffy@ucar.edu`

Abstract

The response of the Pacific Walker circulation (WC) to long-term warming remains uncertain. Here, we diagnose contributions to the WC response in comprehensive and idealized general circulation model (GCM) simulations. We find that the spread in WC response is substantial across both the Coupled Model Intercomparison Project (CMIP6) and the Atmospheric Model Intercomparison Project (AMIP) models, implicating differences in atmospheric models in the spread in projected WC strength. Using a moist static energy (MSE) budget, we evaluate the contributions to changes in the WC strength related to changes in gross moist stability (GMS), horizontal MSE advection, radiation, and surface fluxes. We find that the multimodel mean WC weakening is mostly related to changes in GMS and radiation. Furthermore, the *spread* in WC response is related to the spread in GMS and radiation responses. The GMS response is potentially sensitive to parameterized convective entrainment which can affect lapse rates and the depth of convection. We thus investigate the role of entrainment in setting the GMS response by varying the entrainment rate in an idealized GCM. The idealized GCM is run with a simplified Betts-Miller convection scheme, modified to represent entrainment. The weakening of the WC with warming in the idealized GCM is dampened when higher entrainment rates are used. However, the spread in GMS responses due to differing entrainment rates is much smaller than the spread in GMS responses across CMIP6 models. Therefore, further work is needed to understand the large spread in GMS responses across CMIP6 and AMIP models.

Plain Language Summary

The Walker circulation (WC), an east-west circulation over the tropical Pacific, has an uncertain response to climate warming. We diagnose contributions to the WC response in climate models. We find that the spread in WC responses is similar across atmosphere-only models as across models with both an atmosphere and ocean, implicating the atmosphere in the spread in WC response. We find that the WC response and its spread across models are mostly related to changes in gross moist stability (GMS) and radiation. The GMS measures the propensity of the atmospheric circulation to export energy, and is influenced by the vertical structure of temperature and winds. Changes in atmospheric radiation, especially those associated with clouds, amplify the effects of changes in GMS on the WC.

The GMS is affected by an uncertain parameter in climate models, the entrainment rate. The entrainment rate controls how much clouds mix with their environment. Using an idealized climate model, we learn that the weakening of the WC response is dampened with higher entrainment rates. However, the effect of different entrainment rates is too small to explain the large spread in GMS and WC responses across models; further work is needed to understand this large spread.

1 Introduction

The Pacific Walker circulation (WC) is an atmospheric zonal circulation over the equatorial Pacific Ocean. The WC transports energy from the West Pacific to the East Pacific (Trenberth & Stepaniak, 2003) in response to differing sea surface temperatures (SSTs) and net energy input to the atmosphere over the West and East Pacific. The WC can strongly influence precipitation over the tropical Pacific and also has nonlocal impacts. It is associated with a zonal surface pressure gradient over the Pacific Ocean, whose interannual variability comprises the Southern Oscillation. In addition to influencing the extratropical climate, it can respond to extratropical forcing (Kang et al., 2020). How the WC responds to a warming climate has been assessed using a combination of theory, observations, historical model trends, and model projections. Together, these lines of evidence give an unclear picture of the response of the WC to warming.

Observational and reanalysis products going back only a few decades indicate a strengthening of the WC, while observations over a longer record indicate a weakening (Vecchi et al., 2006; Tokinaga et al., 2012; L'Heureux et al., 2013; Sohn et al., 2016; Wills et al., 2022). This discrepancy may be explained by the large role of internal variability which means that long time periods are needed to evaluate trends in the WC (Vecchi et al., 2006). Coupled climate model trends over the historical period of observed WC strengthening are mixed, with some models indicating a weakening and others indicating a strengthening, though no model strengthens to the same extent as observations (Sohn et al., 2016). Projections of a warm 21st century climate almost unanimously indicate a WC weakening, but with substantial spread in the degree of weakening (Vecchi & Soden, 2007).

There are a number of proposed mechanisms for the response of the WC to warming, some of which suggest a weakening and some of which suggest a strengthening. Tropical convective mass fluxes are constrained to weaken overall with warming because precipitation increases at a slower rate than specific humidity, which increases at a rate set by the Clausius-Clapeyron relationship (Held & Soden, 2006). However, it is not clear that local changes in the WC must follow overall changes in convective mass fluxes (Merlis & Schneider, 2011). Knutson and Manabe (1995) found a weakening of the WC in projections despite an increase in precipitation in the ascent region. Increases in dry static stability, which are the result of changes in moist adiabatic lapse rate, are implicated in this weakening (Knutson & Manabe, 1995; Ma et al., 2012; Sohn et al., 2016). Further, differential increases in evaporative damping between the warm West Pacific and cool East Pacific weaken the SST gradient (Knutson & Manabe, 1995). Additionally, increased CO_2 directly weakens the tropical circulation through differences in masking of the CO_2 radiative forcing by deep clouds and water vapor between tropical ascent and descent regions (Merlis, 2015).

In contrast, an ocean dynamical thermostat mechanism, changes in anthropogenic aerosols, and southern ocean cooling may contribute a strengthening of the zonal SST gradient with warming (Clement et al., 1996; Heede & Fedorov, 2021; Hartmann, 2022). The ocean dynamical thermostat mechanism, which was proposed using a highly idealized ocean model, describes a transient strengthening of the zonal SST gradient through (1) upwelling of relatively cool water in the equatorial East Pacific, thereby increasing the zonal SST gradient, and (2) increases in surface easterly winds which further increase this gradient (Clement et al., 1996). An analysis of coupled GCMs from CMIP3 found the upwelling portion of the mechanism to be operating but not the atmospheric portion of the mechanism because the surface easterly winds tend to weaken in the models, and the net effect is a slight weakening of the zonal SST gradient (DiNezio et al., 2009). Further, analysis of changes in historical CMIP6 simulations from 1950 to 2014 suggests a relative cooling of the equatorial East Pacific due to changes in aerosols, contributing an initial strengthening tendency of the WC (Heede & Fedorov, 2021). Additionally, cooling of the southern ocean is linked with cooling of the tropical East Pacific, and may contribute to the observed strengthening of the zonal SST gradient (Hartmann, 2022).

Here we seek to understand the spread in WC response across GCM projections through an energetic approach. An MSE budget approach has previously been used to study tropical circulations (Neelin & Held, 1987; Chou & Neelin, 2004). We are particularly motivated by the study of Wills et al. (2017) which used a moist static energy (MSE) budget to analyze the response of the WC to warming in simulations with an idealized GCM. Wills et al. (2017) found that the WC strength varies inversely with the gross moist stability (GMS) across a range of climates. GMS measures the efficiency of a circulation in exporting energy (Neelin & Held, 1987; Raymond et al., 2009). GMS has the advantage over the dry static stability, which has previously been used to explain changes in the WC (Knutson & Manabe, 1995; Sohn et al., 2016), that it can account for both dry adiabatic cooling and convective heating associated with ascent, and thus can be used in both the ascent and descent regions of the WC. For a given zonal gradient of net energetic input to the atmosphere, we expect an increase in GMS with warming to correspond to a weaker WC (Wills et al., 2017). In general, we expect the GMS to increase with warming owing predominantly to an increase in tropopause height (Chou et al., 2013). In the observed atmosphere and in more realistic simulations, we expect a more complicated relationship between GMS and WC responses than in the idealized simulations of Wills et al. (2017). Nonetheless, we also find an inverse relationship between WC response and changes in GMS in CMIP6 and AMIP models.

The close relationship we find between the responses of WC strength and GMS across CMIP6 and AMIP simulations warrants further investigation into the response of GMS to warming. We focus on the role of convective entrainment in setting the response of the WC and GMS. In general, entrainment is the process by which a cloud or buoyant plume mixes with the environment. Increasing entrainment affects GMS by (1) steepening the temperature lapse rate and (2) increasing the top-heaviness of vertical velocity profiles (Held et al., 2007; Singh & O'Gorman, 2013; Singh & Neogi, 2022). However, it is difficult to represent entrainment in GCMs because it occurs on subgrid scales and is difficult to measure directly (Romps, 2010). Following Wills et al. (2017), we use an idealized GCM (Frierson et al., 2006; O'Gorman & Schneider, 2008) with a simplified Betts-Miller (SBM) convection scheme (Frierson, 2007) to study the response of the WC to warming. Here we modify the SBM scheme to represent entrainment so that we can evaluate the role of entrainment in the WC and GMS changes across climates.

This paper has two aims: (1) diagnose the contributions to the mean and spread of the WC response to warming in CMIP6 and AMIP simulations using an MSE budget, and (2) evaluate the influence of entrainment on WC strength and its response to warming in simulations with an idealized GCM. We address the first aim in Section 2 and the second aim in Section 3. We discuss and conclude in Section 4.

2 Response of WC to warming in CMIP6 and AMIP simulations

2.1 WC decomposition using GMS and the MSE budget

We diagnose the contributions to the response of the Walker circulation to warming across CMIP6 and AMIP models. We use monthly data of each variable and then take the time and spatial average of calculated terms in a given climate before calculating the difference between warm and control climates. For the CMIP6 simulations, 'control climate' refers to the historical experiment for the years 1970-1999 and 'warm climate' refers to the SSP5-8.5 experiment for the years 2070-2099. For the AMIP simulations, 'control climate' refers to the 'amip' experiment for the years 1979-2014 and 'warm climate' refers to the 'amip-future4K' experiment for the years 1979-2014. The same ensemble member is used for both control and warm experiments. The imposed SST field of the 'amip-future4K' experiment is of a simulated warming, including a change in pattern derived from coupled model experiments. The imposed SST field in 'amip' experiments is the same across models. The imposed SST field in 'amip-future4K' experiments is the same across models. We use one model from each modeling center, matching the AMIP and CMIP6 models where possible. Some models were eventually excluded from the analysis for missing data or excessive spectral ringing. The models used here are shown in Table S1. Tropical-mean skin temperature warming from 20°S to 20°N is used to normalize throughout (i.e., to calculate rates of change in % K^{-1}).

We develop a framework for diagnosing contributions to changes in WC strength using the MSE budget. The WC strength is measured by -$\overline{\omega}_{w-e} = -p_s^{-1} \int \omega_{w-e} dp$ where p_s is surface pressure, ω is vertical velocity in pressure coordinates, the overbar indicates a vertical average in pressure over the depth of the atmosphere, and $w-e$ denotes a horizontal average over a western Pacific box minus a horizontal average over an eastern Pacific box. We use the same boxes as Vecchi et al. (2006) when evaluating the CMIP6 and

AMIP models. That is, both boxes extend from 5°S to 5°N. The western Pacific box extends from 80°E to 160°E and the eastern Pacific box extends from 160°W to 80°W. The western Pacific box includes a small portion of the Indian ocean. WC strength is calculated by taking spatial and time averages of monthly ω to create two profiles: one for the western box and one for the eastern box. These profiles are then vertically integrated and differences between west and east are taken. For figures and results including the idealized GCM, we will refer to 'ascent region' and 'descent region' instead of 'western box' and 'eastern box', but these should be interpreted equivalently.

We difference the MSE budget in the time average between the western and eastern boxes to give

$$\left\langle \omega \frac{\partial h}{\partial p} \right\rangle_{w-e} \approx - \left\langle \mathbf{u} \cdot \nabla h \right\rangle_{w-e} + R_{w-e} + S_{w-e}, \tag{1}$$

where $\langle \cdot \rangle$ indicates a mass-weighted vertical integral, the subscript $w-e$ indicates the difference between western and eastern boxes, $\mathbf{u}$ are horizontal winds, R is the sum of net longwave and shortwave radiative fluxes into the atmosphere (including at both the surface and top of atmosphere), S is the sum of upward surface fluxes of latent and sensible heat, and $h = c_pT + gz + Lq$ is MSE where c_p is the heat capacity of dry air, T is temperature, g is acceleration due to gravity, z is height, L is latent heat of vaporization, and q is specific humidity. All four terms in Equation 1 are implicitly taken to be time averages in a given climate assuming a statistical steady state, and we are neglecting sub-monthly eddy terms, whose differences between climates are small (not shown).

There are numerous definitions of GMS in the literature. Similar to Wills et al. (2017), a definition of GMS appropriate for the WC is used here, denoted $\mathrm{GMS_{WC}}$. $\mathrm{GMS_{WC}}$ is the ratio of vertical advection of MSE, differenced between the western and eastern boxes, to the WC strength and is given by

$$\mathrm{GMS_{WC}} \equiv -g \frac{\left\langle \omega \frac{\partial h}{\partial p} \right\rangle_{w-e}}{\overline{\omega}_{w-e}}. \tag{2}$$

We further introduce $\hat{\omega} = \frac{\omega}{\overline{\omega}_{w-e}}$ as the shape of the vertical-velocity profile to give the simple form

$$\mathrm{GMS_{WC}} = -g \left\langle \hat{\omega} \frac{\partial h}{\partial p} \right\rangle_{w-e}, \tag{3}$$

so that $\mathrm{GMS_{WC}}$ can be thought of as depending on the shape of the vertical velocity profile and the MSE stratification, rather than directly on the WC strength. Our definition of $\mathrm{GMS_{WC}}$ is similar to what Wills et al. (2017) calls GMS or $\mathcal{M}$ with two differences. First, instead of taking a zonal anomaly, we take the difference between the western and eastern Pacific boxes. Second, we use a different definition of WC strength. Wills et al. (2017) defined the WC strength by the zonally-anomalous vertical velocity at the level of its maximum, ω^*_{max}. Instead, we use vertically averaged ω and the difference between the western and eastern Pacific boxes, as described above.

In order to derive a diagnostic expression for WC strength from the MSE budget, we combine Equations 1 and 2 to give

$$-\overline{\omega}_{w-e} \approx g \frac{- \left\langle \mathbf{u} \cdot \nabla h \right\rangle_{w-e} + R_{w-e} + S_{w-e}}{\mathrm{GMS_{WC}}}. \tag{4}$$

Considering a perturbation due to climate change gives an expression for the fractional change in WC strength as a function of changes in $\mathrm{GMS_{WC}}$, horizontal MSE advection, surface heat fluxes, and radiation:

$$\delta \overline{\omega}_{w-e} \approx -\delta \mathrm{GMS_{WC}} - \frac{\Delta \left\langle \mathbf{u} \cdot \nabla h \right\rangle_{w-e}}{\left\langle \omega \frac{\partial h}{\partial p} \right\rangle_{w-e}} + \frac{\Delta R_{w-e}}{\left\langle \omega \frac{\partial h}{\partial p} \right\rangle_{w-e}} + \frac{\Delta S_{w-e}}{\left\langle \omega \frac{\partial h}{\partial p} \right\rangle_{w-e}}. \tag{5}$$

Here and throughout the paper, Δ indicates a response to warming, δ is the fractional response to warming given by $\delta X = \frac{\Delta X}{X}$. We evaluate X in the denominator as the average between the control and warm climates and $\left\langle \omega \frac{\partial h}{\partial p} \right\rangle_{w-e}$ in Equation 5 is also evaluated as the average between the control and warm climates to avoid cross terms. Therefore no additional approximations are introduced between Equations 4 and 5. Equation 5 is evaluated by first calculating the the energy budget terms of Equation 1, then climatologies for each month of the year taken for each term, then differences between climates are taken where applicable, and then spatial and annual means are taken for the western and eastern Pacific boxes. Lastly, the terms in Equation 5 are evaluated. The terms on the RHS of Equation 5 are the contributions to the WC response from changes in $\mathrm{GMS_{WC}}$, horizontal advection, radiation, and surface heat fluxes, respectively. Equations 1, 4, and 5 are approximations to the extent that there are errors due to, for example, finite differencing in calculating advection terms and neglect of sub-monthly eddy terms. The neglect of sub-monthly eddy terms introduces a substantial residual in a given climate (Equation 4) but only a small residual for the differences between climates (Equation 5).

We further decompose the radiation contribution into a contribution from changes in WC strength and a contribution not related to changes in WC strength using a linear regression of radiation as a function of WC strength. The regression is taken across the 12 climatological monthly means for each model and climate and is given by

$$R_{w-e} \approx r_1 \overline{\omega}_{w-e} + R_0, \tag{6}$$

where r_1 and R_0 are regression coefficients. Having fit r_1 and R_0 using the seasonal cycle, we now return to the average over all months in each climate and take the difference between climates to give

$$\Delta R_{w-e} \approx r_1 \Delta\overline{\omega}_{w-e} + \Delta r_1 \overline{\omega}_{w-e} + \Delta R_0. \tag{7}$$

We continue to use averages between control and warm climates for terms that are not differences between climates so that no cross terms are introduced between Equations 6 and 7. The first term on the RHS is interpreted as the contribution to ΔR_{w-e} which is linked with changes in WC strength, and the sum of the last two terms on the RHS is interpreted as the contribution to ΔR_{w-e} which is not linked with changes in WC strength.

2.2 WC response and decomposition in CMIP6

In order to diagnose contributions to changes in WC strength in coupled GCMs, we apply the decomposition given by Equation 5 to each CMIP6 model. Figure 1a shows the decomposition in the multimodel mean and the spread across models, and Figure S1 shows the decomposition in individual CMIP6 models. We find that the WC weakens in all models, with a weakening ranging from a 6% K^{-1} to 20% K^{-1}. The multimodel mean weakening of 12% K^{-1} is greater than the 5 to 10% K^{-1} estimated by Vecchi and Soden (2007) using changes in ω at 500 hPa and this is partly because we normalize by changes in tropical mean SST warming rather than global-mean surface warming as in Vecchi and Soden (2007).

Looking at Figures 1a and S1, we notice that the relative roles of each mechanism in setting the WC response can vary substantially across models, but a few important commonalities emerge. The response of $\mathrm{GMS_{WC}}$ contributes a weakening of the WC in all models. That is, $\mathrm{GMS_{WC}}$ increases with warming in all models, consistent with Chou et al. (2013). The contribution from changes in $\mathrm{GMS_{WC}}$ ranges from a weakening of 4 to 18% K^{-1}. The total radiation contribution also contributes a weakening in all models, ranging from a weakening of 1 to 18% K^{-1}. The total radiation contribution is well approximated by the sum of the WC-linked and not WC-linked portions, with the WC-linked portion dominating in the multimodel mean (Figure 1c). Thus, the weakening contribution from radiation in the multimodel mean is largely due to an amplifying feedback of radiation on WC response (cf. Peters and Bretherton (2005)). Looking at Figure S1, EC-Earth3 is an outlier model for the radiation contribution but it is not an outlier for WC response because this model has a small contribution from GMS changes. If the EC-Earth3 model is neglected, the radiation contribution has a spread of 1 to 11% K^{-1}.

2.3 WC response and decomposition in AMIP

In order to isolate the atmospheric contribution to the spread in WC response, we analyze the response of the WC in AMIP simulations using the 'amip' and 'amip-future4K' experiments. Recall that all of the 'amip' experiments have the same imposed SST distribution as one another and all of the 'amip-future4K' experiments have the same imposed SST distribution as one another, so these experiments isolate the role of the atmosphere in causing intermodel differences independent from differences in SST.

As we did with the CMIP6 models, we apply the decomposition given by Equation 5 to each AMIP model. Figure 1b shows the decomposition in the multimodel mean and the spread across models, and Figure S2 shows the decomposition in individual AMIP models. Even with the same SST response across models, there is spread in the weakening response of the WC from 8 to 20% K^{-1} which is similar to the range for the CMIP6 simulations which are coupled with interactive oceans. Similar to the CMIP6 simulations, the WC response is dominated by changes in GMS_{WC} and radiation; both contribute a weakening in all AMIP simulations. The contribution from changes in GMS_{WC} range from a weakening of 6 to 19% K^{-1}, while the contribution from changes in radiation range from a weakening of 3 to 8% K^{-1}. The range of radiation contributions is not much smaller than that of the CMIP6 models when the outlier EC-Earth3 model, which does not appear in AMIP, is removed from CMIP6. Further, the radiation contribution is dominated by changes in the WC-linked portion in the multimodel mean (Figure 1d). The spread due to changes in surface heat fluxes is larger in AMIP than in CMIP6, which may be the result of artificially imposing SSTs. While the substantial spread in WC response across AMIP models does not rule out some role for the ocean in setting the spread in CMIP6, it does suggest an important role of the atmosphere in setting the spread in CMIP6 response.

2.4 Models with CMIP and AMIP equivalents

Our results so far indicate that the spread in WC responses across CMIP6 models is comparable to the spread across AMIP models. However, the two ensembles consist of different sets of models. There are nine models with both AMIP and CMIP6 counterparts. Figure 2 compares the WC responses for these nine models. The WC responses are positively correlated between AMIP and CMIP6 with a correlation coefficient of 0.33. The positive correlation suggests atmospheric processes active in AMIP are contributing to some of the spread in CMIP6 models. Further, the models are evenly distributed above and below the one-to-one line, which suggests that there is not a single mechanism associated with ocean-atmosphere coupling, such as the Bjerknes feedback, causing differences of a consistent sign between CMIP6 models and their AMIP counterparts.

2.5 Contributions of western and eastern boxes

We also decompose each term in Equation 5 into contributions from changes over the West and East Pacific. Figure S3 shows this decomposition for CMIP6 models, and Figure S4 shows this decomposition for AMIP models. In both CMIP6 and AMIP models, changes in $\delta\overline{\omega}_{w-e}$ have weakening contributions from changes over both the West and East Pacific, with a larger contribution from the East Pacific in the multimodel mean.

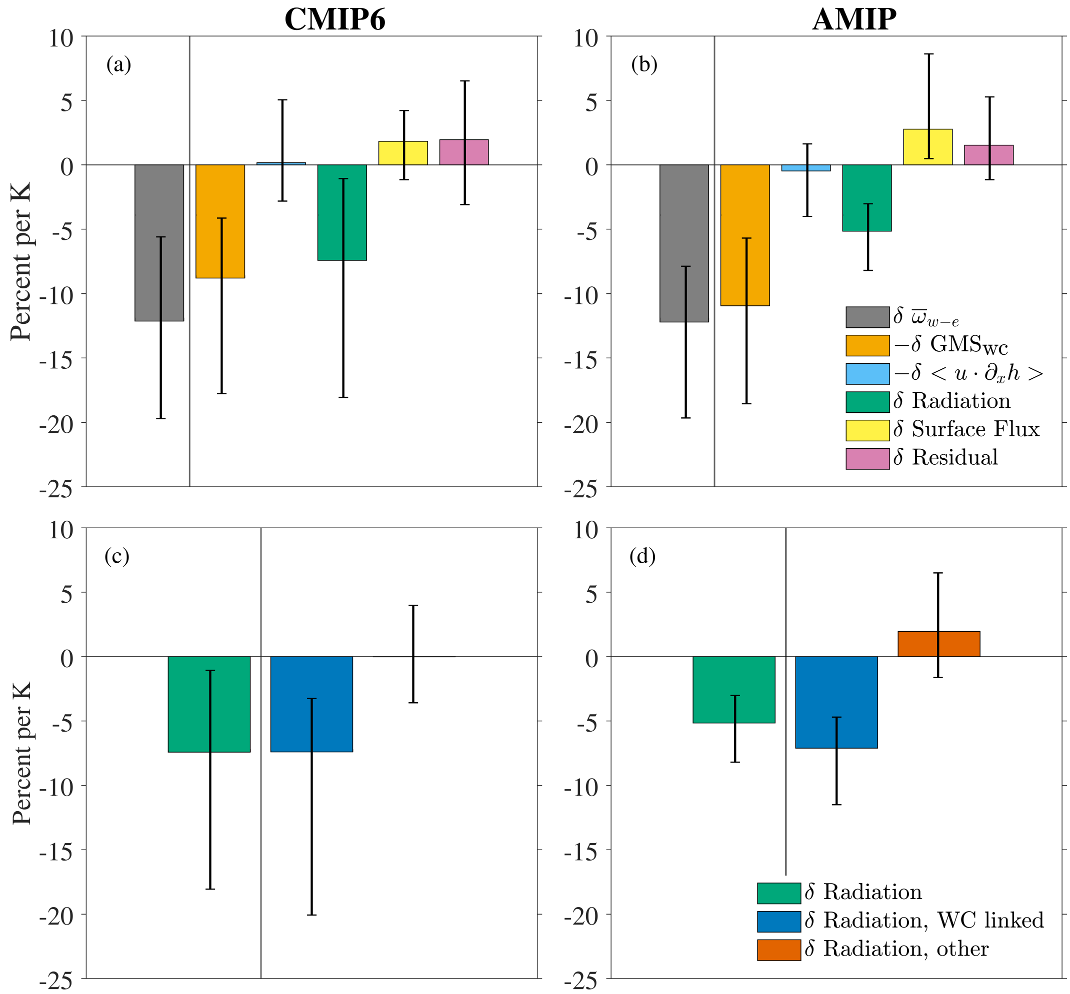

Figure 1. Contributions to multimodel mean response of WC to warming in (a) CMIP6 and (b) AMIP simulations. WC response (gray) is the sum of the contributions from each term on the RHS of Equation 5. The radiation contribution in (c) CMIP6 and (d) AMIP is decomposed into the portion that is linked to WC strength (dark blue) and the portion that is not linked with WC strength (dark orange). The radiation decomposition is performed using the seasonal cycle and Equation 7. The whiskers cover the entire spread across models for each term.

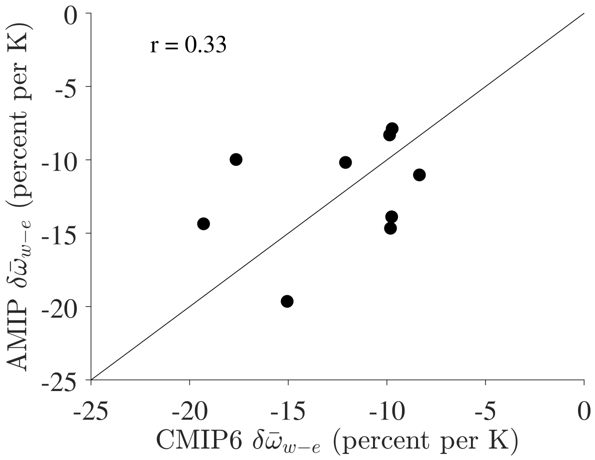

Figure 2. Scatterplot of WC responses in CMIP6 and AMIP simulations for the nine models that are present in both ensembles. The black line is a reference line with a slope of 1.

In both ensembles, the radiation response over the West Pacific contributes a weakening in all models and the GMS response over the East Pacific contributes a weakening in all models. GMS also contributes a weakening over the West Pacific in the multimodel mean and in most models. The radiation contribution over the East Pacific is uncertain.

2.6 Relationship between WC and GMS responses

Given their large contributions, we investigate the roles of changes in GMS_{WC} and radiation on WC strength in the remainder of Section 2.

We expect GMS_{WC} to vary inversely with WC strength because a larger increase in GMS indicates a larger weakening of the atmospheric circulation for a given energetic forcing. Figure 3 shows that the relationship between responses of WC strength and GMS_{WC} in CMIP6 and AMIP models are consistent with this expectation: the WC weakens and GMS_{WC} increases in all models, with a tendency for greater weakening of the WC with a greater increase in GMS_{WC}. The correlation coefficient is -0.71 across the CMIP6 models and -0.91 across the AMIP models. Most models fall below the line through the origin with a slope of -1 because changes in radiation also contribute to a weakening of the Walker circulation. There is a greater spread in the radiation contribution across CMIP6 models than AMIP models (Figure 1), so the correlation between GMS_{WC} response and WC response is lower across CMIP6 models than across AMIP models. The outlier CMIP6 model located near (6,-20) is EC-Earth3, which has the largest radiation contribution of any CMIP6 model (Figure S1).

Figure 3 also shows a measure of the standard error of the WC response for each model. The WC response in Figure 3 is shown as the fractional change in WC strength normalized by surface temperature response, given by $100\left(\frac{\Delta\bar{\omega}_{w-e}}{\bar{\omega}_{w-e}}\right)/\Delta T_s$. We calculate the standard error of the change in WC strength, $\Delta\bar{\omega}_{w-e}$, as $\frac{\sqrt{\mathrm{std}(\bar{\omega}_{w-e}^{warm})^2+\mathrm{std}(\bar{\omega}_{w-e}^{ctrl})^2}}{\sqrt{n}}$, where n is the number of simulation years in each climate and $std()$ indicates a standard deviation across model years. This standard error calculation assumes WC strength is independent between different model years and climates. We then normalize by multiplying by $100/\left(\bar{\omega}_{w-e}/\Delta T_s\right)$ so that the standard error has the same units as the plotted value. The standard errors are sufficiently small that we can be sure that the intermodel spread in WC response is not just due to unforced variability.

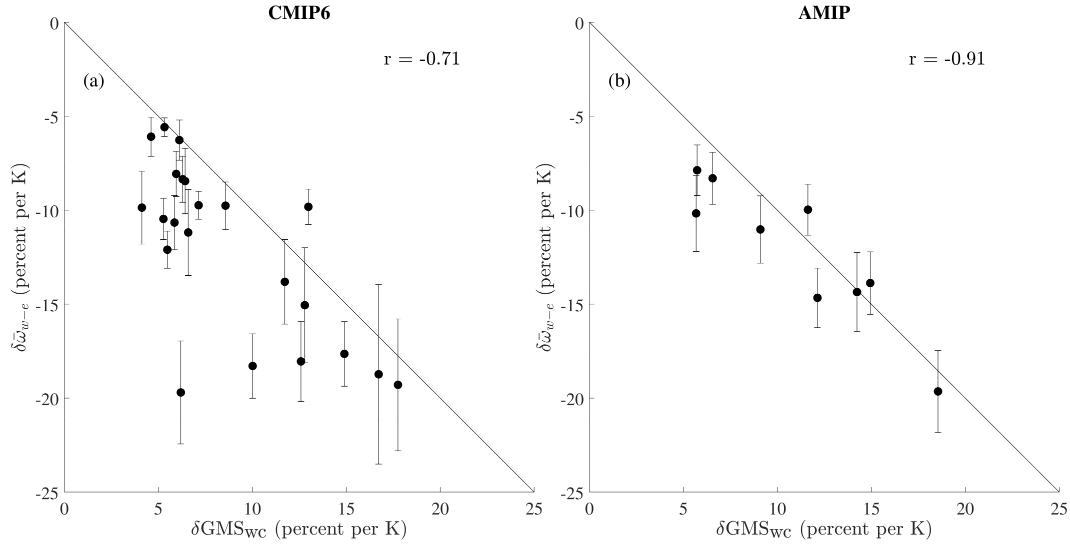

Figure 3. Relationship between responses of $\mathrm{GMS_{WC}}$ and WC strength for (a) CMIP6 and (b) AMIP simulations. The error bars indicate a measure of the standard error of the WC response calculated as described in Section 2.6. The black lines are reference lines with slopes of -1.

Wills et al. (2017) showed a similar inverse relationship between WC strength and GMS in idealized GCM simulations. The strong anticorrelation between responses of WC strength and $\mathrm{GMS_{WC}}$ indicates that the WC-GMS relationship holds in more complex simulations and warrants further investigation into the response of $\mathrm{GMS_{WC}}$ to warming.

2.7 $\mathrm{GMS_{WC}}$ decomposition

In order to better understand the response of $\mathrm{GMS_{WC}}$ to warming in CMIP6 and AMIP models, we decompose the $\mathrm{GMS_{WC}}$ response into contributions due to changes in vertical velocity and MSE profiles. Looking at Equation 3, the fractional change in $\mathrm{GMS_{WC}}$ with warming has contributions from changes in the shape of the vertical velocity profile $\hat{\omega}$ and changes in the MSE profile through $\partial h/\partial p$ as follows:

$$\delta\mathrm{GMS_{WC}} \approx \frac{\left\langle \Delta\hat{\omega}\frac{\partial h}{\partial p}\right\rangle_{w-e}}{\left\langle \hat{\omega}\frac{\partial h}{\partial p}\right\rangle_{w-e}} + \frac{\left\langle \hat{\omega}\Delta\frac{\partial h}{\partial p}\right\rangle_{w-e}}{\left\langle \hat{\omega}\frac{\partial h}{\partial p}\right\rangle_{w-e}}. \tag{8}$$

There is a small residual because monthly climatologies of $\hat{\omega}$ and $\partial h/\partial p$ are used in calculating the numerator.

Figures 4a,b,d,e compare ascent-region MSE profiles and their response to warming in CMIP6 and AMIP models. The response of surface MSE is subtracted from each response profile since it is the vertical gradient of MSE which affects GMS. For the CMIP6 and AMIP models, profiles are averaged over the area of the western Pacific box. Figures 5a,b,d,e compare $\hat{\omega}$ profiles and their response to warming. All response profiles are normalized by tropical-mean SST warming. Figure 4 reveals that MSE increases with warming and Figure 5 reveals that $\hat{\omega}$ profiles have a tendency to shift upward with warming consistent with the increase in tropopause height and the upward shift of the general circulation with warming (Singh & O'Gorman, 2012).

The results of the decomposition of $\delta\mathrm{GMS_{WC}}$ from Equation 8 are shown for the multimodel means in Figure 6, for each CMIP6 model in Figure S5, and for each AMIP

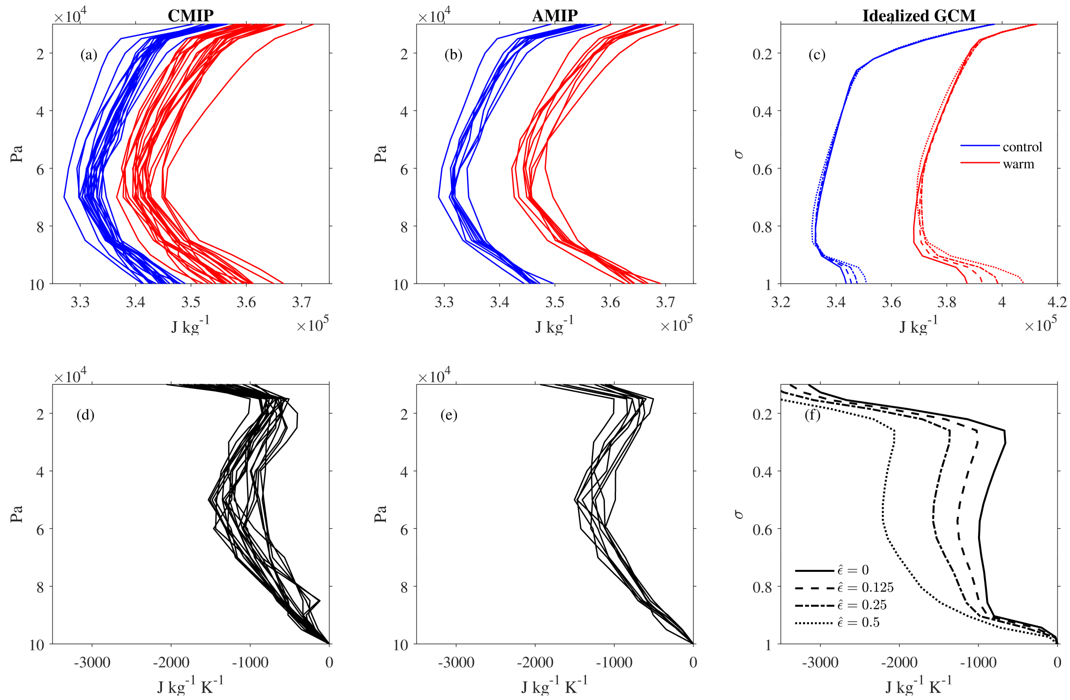

Figure 4. Ascent-region MSE profiles (a-c) and their response to warming (d-f) in CMIP6 (a,d), AMIP (b,e), and the idealized GCM (c,f). In panels (d-f), surface MSE responses for each profile is subtracted so that all profiles go through zero at the surface. The response profiles (d-f) are normalized by the tropical-mean SST response. CMIP6 and AMIP profiles are in pressure coordinates and idealized profiles are in sigma coordinates. CMIP6 and AMIP profiles are averaged over the ascent region of the WC defined here as the western box, and idealized GCM profiles are averaged over the boundary of the ascent region to be consistent with the boundary $\mathrm{GMS_{WC}}$ introduced in Section 3.5 (see text for details).

model in Figure S6. The $\hat{\omega}$ contribution is positive and considerably larger in magnitude than the MSE profile contribution for both CMIP6 and AMIP. The positive contribution from changes in $\hat{\omega}$ is consistent with the increase in GMS from increasing tropopause height and the associated upward shift of $\hat{\omega}$ (Chou et al., 2013; Wills et al., 2017). We also see a partially-compensating negative contribution from changes in MSE profile. Changes in MSE profile are also influenced by the upward shift. Not taking into account the upward shift in all variables simultaneously is a limitation of the decomposition used here.

Using the definition of $h = c_pT + gz + Lq$, the h profile contribution can be linearly decomposed into contributions from changes in temperature (T), geopotential height (z) and specific humidity (q). Further, the changes in specific humidity can be decomposed into its contributions from changes in saturation specific humidity (q_{sat}) and relative humidity (RH), according to $\Delta q \approx \Delta \mathrm{RH}\, q_{sat} + \mathrm{RH}\, \Delta q_{sat}$, where again there is a small residual since climatologies of each term are used. Figures 6, S2, and S4 show that changes in h profile tend to have small net contributions to changes in $\mathrm{GMS_{WC}}$, but this is the result of compensation between strong positive contributions from changes in T and Φ and a strong negative contribution from changes in specific humidity. The contribution from changes in specific humidity, which acts to decrease the $\mathrm{GMS_{WC}}$, is mostly the result of changes in saturation specific humidity. Note that our contributions from changes in T, z, and q assume constant $\hat{\omega}$, and thus our contributions differ from the contributions found in Wills et al. (2017) in which the increase in tropopause height was in-

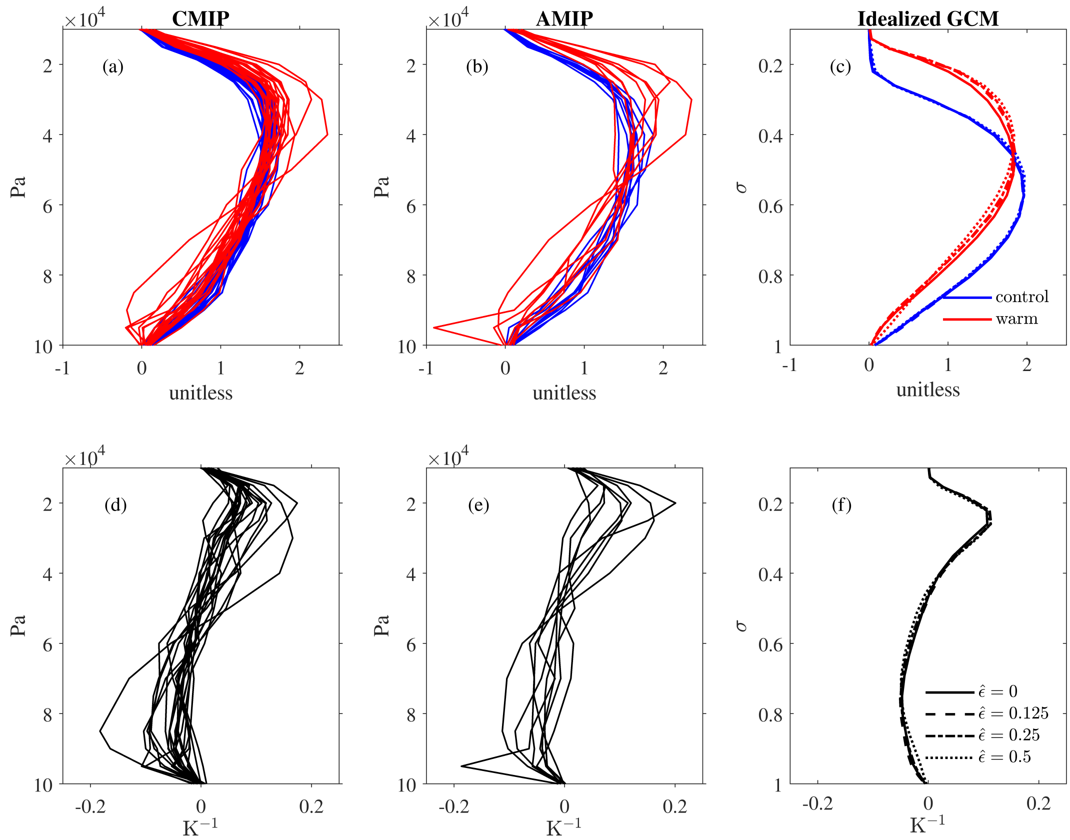

Figure 5. Profiles of $\hat{\omega}$ (a-c) and their response to warming (d-f) in CMIP6 (a,d), AMIP (b,e), and the idealized GCM (c,f). The response profiles (d-f) are normalized by the tropical-mean SST response. CMIP6 and AMIP profiles are in pressure coordinates and idealized GCM profiles are in sigma coordinates. All profiles represent the average over the ascent region minus the average over the descent region (see text for details). For the CMIP6 and AMIP simulations, the ascent and descent regions are the western and eastern boxes, respectively.

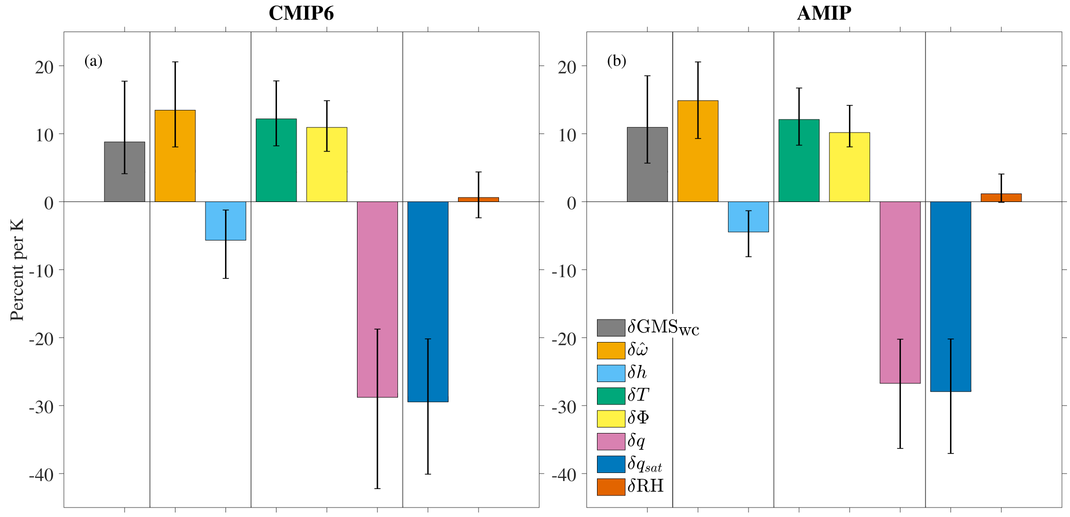

Figure 6. Contributions to the multimodel mean response of $\mathrm{GMS_{WC}}$ to warming in (a) CMIP6 and (b) AMIP simulations. The response of $\mathrm{GMS_{WC}}$ to warming (gray) is decomposed into contributions from changes in shape of vertical velocity profile (light orange) and changes in MSE (light blue) as in Equation 8. The MSE contribution is further decomposed into contributions from changes in temperature (green), geopotential height (yellow), and humidity (pink). The humidity contribution is further decomposed into contributions from changes in saturation specific humidity (dark blue) and relative humidity (dark orange). The whiskers cover the entire spread across models for each term.

cluded. Figure 6 also shows that intermodel spread in changes in both the MSE profile and the shape of the vertical velocity profile contribute to the intermodel spread in the GMS response.

2.8 Relationship between WC and radiation responses

Radiation responses contributes a weakening of the WC in all AMIP and CMIP models. Figures 1c,d show that the WC-linked portion of the radiation response dominates over the portion not linked with the WC. We further decompose the radiation contribution into top of atmosphere (TOA) and surface contributions, SW and LW contributions, and clear-sky and cloud-radiative effects (CRE), for a total of eight terms (Figures S7 and S8). We further decompose these eight terms into their WC-linked and other contributions by adapting the regression used for Figure 1 (Figures S9 and S10).

Across CMIP6 and AMIP models, CRE dominates over clear-sky contributions in both magnitude and spread across models. In particular, the CRE of TOA LW, TOA SW, and surface SW are dominant with the largest intermodel spread. For each of these three contributions, the WC-linked portion dominates across CMIP6 and AMIP models. These results suggest that changes in clouds associated with the WC dominate the spread in the radiation contribution across models and, in general, amplify the weakening of the WC with warming in models. That the radiation and circulation influence one another is consistent with the findings of Peters and Bretherton (2005) and Silvers and Robinson (2021).

Keeping in mind that cloud-radiative effects amplify the WC response, we next further investigate changes in $\mathrm{GMS_{WC}}$, which is the other primary contributor to the WC response. In particular, we examine the effect of convective entrainment in the $\mathrm{GMS_{WC}}$

response given that convective entrainment can affect both the MSE profile and the shape of the vertical velocity profile.

3 The role of entrainment in setting GMS and WC strength in idealized GCM simulations

3.1 Why consider entrainment?

In order to further evaluate the spread in WC strength response, we study the role of entrainment in setting the WC strength and its response to warming in an idealized GCM. Entrainment is a parameterized process which is difficult to quantify in observations. However, entrainment can have a substantial effect on the climate, especially in the tropics (Singh & O'Gorman, 2013; Miyawaki et al., 2020). Entrainment affects the temperature lapse rate: a higher entrainment rate tends to steepen the temperature lapse rate in the lower and mid troposphere in GCM simulations (Held et al., 2007; Keil et al., 2021). Variations in temperature lapse rate with entrainment will also affect specific humidity, and both the temperature and humidity profiles influence the MSE profile, a key portion of the GMS. Further, entrainment can increase the top-heaviness of vertical velocity profiles (Singh & Neogi, 2022) which again strongly influences the GMS (Inoue et al., 2021). Therefore, we test the effect of entrainment on the GMS and WC using idealized simulations with different values of an entrainment parameter. These idealized simulations allow us to establish a causal relationship between imposed changes in stratification (from changes in entrainment) and the effect on GMS and WC strength, and are thus complementary to the CMIP6 and AMIP results which are diagnostic. Other processes such as radiation also contribute to differences in the WC response and should be studied in future work.

3.2 Idealized GCM simulations

Idealized simulations of the Walker circulation are run using an idealized moist atmospheric GCM based on the GFDL spectral dynamical core following Frierson et al. (2006) with details as in O'Gorman and Schneider (2008). The idealized GCM lacks land, a seasonal cycle, and cloud and water-vapor radiative feedbacks. The lower boundary is a thermodynamic mixed-layer ocean with a depth of 1 m. The horizontal convergence of the ocean energy flux is specified through a Q flux. There is a zonal-mean component of the Q flux with a maximum magnitude of 30 W m^{-2} and a latitudinal width parameter of 16° following Equation 1 of Merlis and Schneider (2011). Through missing a cosine latitude factor, this zonal-mean Q flux formulation induces a small global-mean sink of energy (Merlis et al., 2013) which is not expected to strongly affect the results presented here.

Following Wills et al. (2017), the WC is driven by a zonally anomalous component of the Q flux with an elliptic convergent region in the 'western' hemisphere (leading to atmospheric ascent) and an equal and opposite divergent region (leading to atmospheric descent) in the 'eastern' hemisphere, both centered on the equator. The zonally anomalous Q flux, Q^*, has the form

$$Q^* = Q_1 \exp\left[-\frac{(\lambda-\lambda_W)^2}{2\sigma_\lambda^2} - \frac{\phi^2}{2\sigma_\phi^2}\right] - Q_1 \exp\left[-\frac{(\lambda-\lambda_E)^2}{2\sigma_\lambda^2} - \frac{\phi^2}{2\sigma_\phi^2}\right], \tag{9}$$

where λ is longitude, ϕ is latitude, $Q_1 = 50$ W m^{-2} is the amplitude of the zonally anomalous Q flux, $\lambda_E = 270°$ is the longitude of the center of the descent region, $\lambda_W = 90°$ is the longitude of the center of the ascent region, $\sigma_\lambda = 12.5°$ is proportional to the zonal extent of the anomaly, and $\sigma_\phi = 8°$ is proportional to the meridional extent of the anomaly. The sign of the zonally anomalous Q flux is modified from Wills et al. (2017) such that positive indicates a flux from ocean to atmosphere at steady state. The imposed zonally anomalous Q flux is plotted in Figure S11. We define the ascent region as the elliptic area within the 10 W m^{-2} Q-flux contour and the descent region as the elliptic area within the -10 W m^{-2} Q-flux contour. We refer to these as 'west' and 'east' and continue to use the $w-e$ subscript because the ascent region is meant to represent the West Pacific and the descent region is meant to represent the East Pacific.

The idealized simulations are spun up for four years, and the analysis is performed on the following eight years of simulation output. The convection scheme is a modification of the simplified Betts-Miller (SBM) convection scheme of Frierson (2007), which relaxes temperature profiles to a moist adiabat and relative humidity to 70% in convecting regions. Here, we modify the SBM scheme by introducing a non-dimensional entrainment parameter $\hat{\epsilon}$ such that the convection scheme relaxes to the temperature profile of an *entraining* plume when $\hat{\epsilon} > 0$. Our entraining SBM scheme reduces to the SBM convection scheme when $\hat{\epsilon} = 0$. Details about the modification to represent entrainment are given in Appendix A.

The longwave optical depth distribution is specified as a function of latitude and pressure and then scaled by a factor α (O'Gorman & Schneider, 2008). Two climates are simulated: a control climate with a default longwave optical depth ($\alpha = 1$) and a warm climate with doubled longwave optical depth ($\alpha = 2$). From the control to the warm climate there is a large warming with a global-mean SST increase of 11.2K and a tropical-mean (20°S to 20°N) SST increase of 9.1K in the simulations without entrainment. We also considered additional α values and, consistent with Wills et al. (2017), we found that WC strength scales nearly linearly with temperature. Therefore, it is reasonable to compare our results (when normalized per K) to the CMIP6 and AMIP models with less warming. The ocean Q flux is held constant as the climate warms. We run the idealized model for simulations of a control climate and a warm climate with four values of the entrainment parameter $\hat{\epsilon}$, for a total of eight simulations. The four values of $\hat{\epsilon}$ are 0 (no entrainment), 0.125, 0.25, and 0.5.

3.3 Spread in MSE and $\hat{\omega}$ profiles

Before evaluating responses of WC strength and GMS to warming across entrainment rates in the idealized GCM, it is useful to examine the $\hat{\omega}$ and MSE profiles and their responses to warming (Figures 4 and 5) since these affect the GMS response. Figure 4 compares the ascent-region MSE profiles and their responses to warming in CMIP6 models, AMIP models, and across entrainment rates in the idealized GCM. Recall that the response of surface MSE is subtracted from each profile since it is the vertical gradient of MSE which affects GMS. For the idealized GCM, MSE profiles are averaged over the *boundary* of the elliptic ascent region, consistent with the upcoming GMS analysis. Note that the gray radiation scheme used in the idealized GMS leads to biases in vertical temperature structure as compared to more complex radiation schemes (Tan et al., 2019). These biases likely influence the MSE profiles in Figures 4c,f. Figure 5 compares $\hat{\omega}$ profiles and their responses to warming in CMIP6 models, AMIP models, and across entrainment rates in the idealized GCM. Recall that response profiles are normalized by tropical-mean SST warming.

Focusing on the sensitivity to entrainment in the idealized GCM, Figures 4c and 5c show that entrainment has a bigger effect in the warmer climate than in the control climate. The greater sensitivity to entrainment in a warmer climate is because entrainment in the convection scheme acts on the difference between the MSE of the environment and that of saturated rising air, and this difference is larger in the warm climate. Figure 4c reveals that increases in entrainment have a tendency to steepen the MSE lapse rate, especially in the lower troposphere, and that this steepening is greater in the warmer climate. Figure 5c reveals that $\hat{\omega}$ profiles have a tendency to shift upward with warming, and this upward shift is enhanced by convective entrainment. The enhancement in the upward shift of $\hat{\omega}$ with higher entrainment rates is broadly consistent with Singh and Neogi (2022), who found that entrainment tends to make vertical velocity profiles more top heavy.

Comparing the idealized GCM to CMIP6 and AMIP, we find some important similarities in the response to warming including an increase in MSE, a steeping of the lapse rate of MSE in the lower troposphere, and an upward shift of the $\hat{\omega}$ profile. We also find that the spread in MSE profile response across entrainment rates in the idealized GCM is substantial and somewhat larger than the spread in MSE profile response across CMIP6 and AMIP models. We hypothesize that the sensitivity to entrainment in the upper troposphere may be exaggerated because the convection scheme used in the idealized simulation is based on a single plume with one fixed entrainment profile, whereas with a spectrum of plumes the air that reaches the upper-troposphere is only weakly affected by entrainment. Interestingly, the spread across control-climate MSE profiles in CMIP6 and AMIP models is larger than the spread across entrainment rates in the idealized GCM, but the opposite is true for the response of MSE profiles to warming. In contrast to the MSE profiles, we find that the spread in $\hat{\omega}$ profile response across entrainment rates in the idealized simulations is very small as compared to the spread in CMIP6 and AMIP simulations. Thus we expect $\hat{\omega}$ changes to play a much bigger role for the spread in GMS and WC response in CMIP6 and AMIP compared to the variation across entrainment rates in the idealized GCM simulations.

3.4 Sensitivity of WC strength to warming and entrainment in idealized simulations

The WC strength is defined as the negative of the average value of ω in the ascent region minus the average value of ω over the descent region. Further, we estimate the uncertainty in WC strength by using the WC strength in each of the eight simulated years to calculate the standard error for the eight-year average. The WC strength and its standard error are plotted in Figure 7a for each of the idealized GCM simulations. In general, the WC is weaker in the warm climate than in the control climate, consistent with the CMIP6 and AMIP simulations. WC strength increases with increasing entrainment in both climates, but the sensitivity to entrainment is greater in the warm climate. As a result, the WC weakens with warming more at lower entrainment rates than it does at higher entrainment rates. While entrainment does affect the response of the WC to warming, the spread due to variations in entrainment of 1.6% K^{-1} (Figure 8) is not as large as the spread due to differences across models in CMIP6 (14% K^{-1}) or AMIP (12% K^{-1}). Figures 4 and 5 suggest that this is because variations in entrainment only capture the size of the spread in MSE profile response, but not the size of the spread in $\hat{\omega}$ response. Further, this may be partly because radiative feedbacks are not as fully represented in the idealized model as they are in the CMIP6 and AMIP models, and our analysis in Sections 2.2 and 2.3 suggests that they have an amplifying effect on the WC response.

3.5 GMS in idealized simulations

From Wills et al. (2017), the Walker circulation strength varies inversely with a GMS measure similar to $\mathrm{GMS_{WC}}$ in this idealized GCM when entrainment is set to zero. Here we determine whether this relationship between WC strength and GMS responses holds with variations in entrainment. Looking at Equation 1, we notice that in the idealized simulations the sum of changes in R_{w-e} and S_{w-e} is negligible because the Q flux at the surface is fixed and changes in radiation are very nearly zonally uniform because the simulations do not have cloud-radiative effects or water vapor-radiative feedback. Therefore, the radiative and surface flux terms vanish from Equations 1 and 5 when applied to the idealized simulations. Consequently, in the idealized simulations, Equation 5 re-

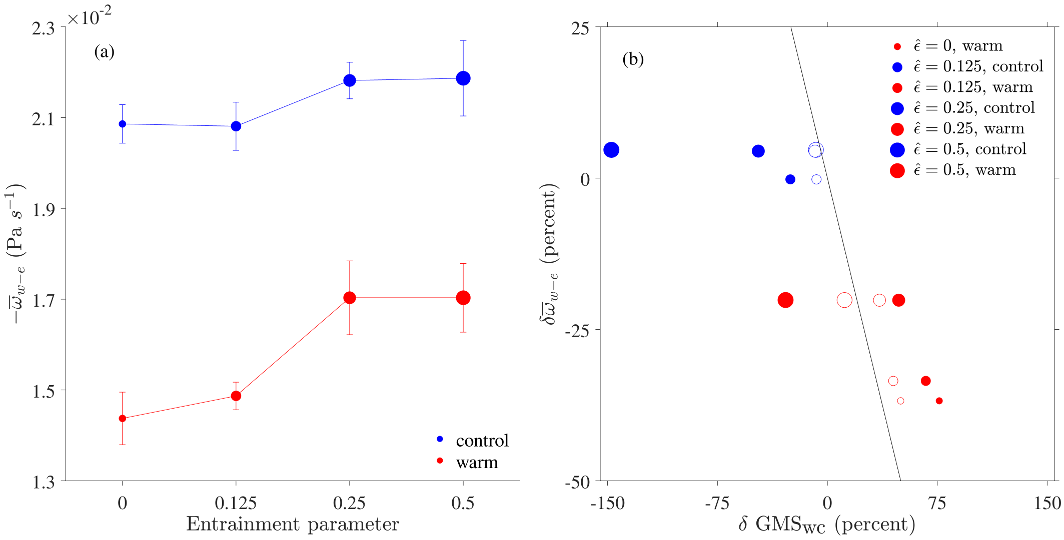

Figure 7. (a) WC strength versus entrainment for a control climate with default longwave optical depth (blue) and a warm climate with double longwave optical depth (red) in the idealized GCM simulations. Error bars show the standard error. (b) Relationship between GMS$_{\mathrm{WC}}$ response and WC response to warming and changes in entrainment in the idealized GCM simulations. Delta indicates the fractional change from the reference case of the control climate ($\alpha = 1$) with zero entrainment ($\hat{\epsilon} = 0$). Filled circles indicate the response of GMS$_{\mathrm{WC}}$ and open circles indicate the response of boundary GMS$_{\mathrm{WC}}$, where boundary GMS$_{\mathrm{WC}}$ is defined by Equation 11. Black line is a reference line with slope of -1. Blue symbols indicate that the perturbed climate is a control climate and red symbols indicate that the perturbed climate is a warm climate.

duces to

$$\delta\overline{\omega}_{w-e} \simeq -\delta \mathrm{GMS}_{\mathrm{WC}} - \frac{\Delta \left\langle \mathbf{u} \cdot \nabla h \right\rangle_{w-e}}{\left\langle \omega \frac{\partial h}{\partial p} \right\rangle_{w-e}}, \tag{10}$$

where δ is a fractional response and Δ is a difference between simulations in response to warming or changes in entrainment parameter. Equation 10 is an excellent approximation, and thus there is an inverse relationship between WC strength and GMS$_{\mathrm{WC}}$ if changes in the horizontal MSE advection term are small.

To evaluate the role of horizontal MSE advection, we compare changes in WC strength and GMS$_{\mathrm{WC}}$. Figure 7b shows that GMS$_{\mathrm{WC}}$ response does not have the expected inverse relationship with WC response (although this does hold approximately for the zero entrainment case that was also considered by Wills et al. (2017)), indicating that changes in horizontal advection terms are important in Equation 10. This is problematic because although we have some understanding of how entrainment affects the vertical MSE advection term through MSE and vertical velocity profiles, we do not have a similar understanding for horizontal MSE advection. In order to reduce the role of horizontal advection in our analysis, we define a version of GMS$_{\mathrm{WC}}$ appropriate for the WC in our idealized simulations called the "boundary GMS$_{\mathrm{WC}}$."

The boundary GMS$_{\mathrm{WC}}$ is defined using MSE averaged over the *boundaries* of the WC ascent and descent regions which are defined in our idealized simulations based on contours of the zonally anomalous Q flux (Q^*). Between the surface and top of atmosphere, the Q^* contours create an elliptic cylinder for each region. We define h_b as the average value of h around the elliptic contour at each level and each time, so that h_b does not vary in latitude or longitude. The boundary $\mathrm{GMS_{WC}}$, or $\mathrm{GMS^b_{WC}}$ is then defined as

$$\mathrm{GMS^b_{WC}} = -g\frac{\left\langle \omega \frac{\partial h_b}{\partial p} \right\rangle_{w-e}}{\overline{\omega}_{w-e}}. \tag{11}$$

Only MSE is averaged over the boundary to give h_b. Terms with the subscript $w-e$ are averaged over the areas of the elliptic ascent and descent regions. Intuitively, boundary $\mathrm{GMS_{WC}}$ is helpful because it removes the effect of horizontal variations within the ascent and descent regions and focuses on the MSE variations on the boundaries of the ascent and descent regions that matter for export and import of energy out of and in to these regions.

To further see why the boundary $\mathrm{GMS_{WC}}$ is helpful, we decompose h at a given vertical level as the sum of h_b and a residual, h' such that $h = h_b + h'$. Considering the ascent region, the advection terms can now be written

$$\left\langle \omega \frac{\partial h}{\partial p} \right\rangle_w + \langle \mathbf{u} \cdot \nabla h \rangle_w = \left\langle \omega \frac{\partial h_b}{\partial p} \right\rangle_w + \left\langle \omega \frac{\partial h'}{\partial p} \right\rangle_w + \langle \mathbf{u} \cdot \nabla h' \rangle_w , \tag{12}$$

where we have used that h_b does not vary horizontally. A similar result holds for the descent region. In order for $\left\langle \omega \frac{\partial h_b}{\partial p} \right\rangle_w$ to dominate the right-hand side, we need h' advection, $\left\langle \omega \frac{\partial h'}{\partial p} \right\rangle_w + \langle \mathbf{u} \cdot \nabla h' \rangle_w = \langle \nabla_{\mathrm{3d}} \cdot (\mathbf{u}_{\mathrm{3d}} h') \rangle_w$, to be negligible. By the divergence theorem, this will be the case if $\mathbf{u}_{\mathrm{3d}} h'$ is close to zero on the boundary of the elliptic cylinder, which will be the case if h' is close to zero on this boundary, meaning that the h contours at each vertical level align with the -10 and 10 W m^{-2} surface Q^* contours used to define the boundary. At latitudes near the equator, we expect the h contours to roughly align with the Q^* contours because Q^* is forcing anomalous warming and moistening in the ascent region and anomalous cooling and drying in the descent region. If this is approximately the case, then Equation 12 and the equivalent for the descent region gives that

$$\left\langle \omega \frac{\partial h}{\partial p} \right\rangle_{w-e} + \langle \mathbf{u} \cdot \nabla h \rangle_{w-e} \simeq \left\langle \omega \frac{\partial h_b}{\partial p} \right\rangle_{w-e}. \tag{13}$$

Continuing to assume that h' is close to zero on the boundary of the elliptic cylinder and repeating the derivation of Equation 10 but using $\mathrm{GMS^b_{WC}}$ gives that

$$\delta\overline{\omega}_{w-e} \simeq -\delta\mathrm{GMS^b_{WC}}. \tag{14}$$

We evaluate the extent to which Equations 13 and 14 hold by looking at Figure 7b. We can see that the relationship between WC response and boundary $\mathrm{GMS_{WC}}$ response is much closer to the slope -1 line than the relationship between WC response and $\mathrm{GMS_{WC}}$. The extent to which the WC and boundary $\mathrm{GMS_{WC}}$ responses depart from the slope -1 line is due almost entirely to the neglect of h' advection because Equation 10 is nearly exact in the idealized simulations.

Our results show that the boundary $\mathrm{GMS_{WC}}$ is a better metric than $\mathrm{GMS_{WC}}$ for understanding the WC response across entrainment rates and climates in the idealized GCM. By contrast, it was sufficient to use the $\mathrm{GMS_{WC}}$ in the analysis of the CMIP6 and AMIP simulations. Horizontal MSE advection does provide a contribution in the CMIP6 and AMIP simulations, but the multimodel mean of this contribution is close to zero and the model spread is not as big as the spread in the $\mathrm{GMS_{WC}}$ contribution (Figures 1a,b). The lesser role for the horizontal advection term in the CMIP6 and AMIP simulations may be because of differences in the structure of the WC. For example, the lesser role may be because of differences in the pattern of heat fluxes for the warm pool as compared to the elliptical anomaly in the idealized simulations or because the range of entrainment parameters is not as wide across CMIP6 and AMIP models as across the idealized GCM simulations.

3.6 Boundary GMS_WC response to warming and decomposition

Finally, we evaluate the response of boundary GMS_WC to warming and compare it to the response of the WC. Looking at Figure 8, we find that the responses of boundary GMS_WC and WC strength are of opposite sign, consistent with the inverse relationship found in Wills et al. (2017) and in the CMIP6 and AMIP models in Sections 2.2 and 2.3 (although those results used GMS_WC rather than boundary GMS_WC). Further, both the weakening of the WC and the increase in boundary GMS_WC with warming dampen with increasing entrainment rate. However, the decreases in WC strength are mostly smaller than the increases in boundary GMS_WC, and this reflects that the boundary GMS_WC does not fully account for contributions from changes in the horizontal MSE advection.

We decompose the response of boundary GMS_WC to warming in the idealized simulation as was done in Section 2.7 but here we replace GMS_WC with boundary GMS_WC in Equation 8. Similar to the CMIP6 and AMIP results, the $\Delta\hat{\omega}$ contribution is positive and larger in magnitude than the negative Δh contribution (Figure 9). The Δh contribution is again the result of compensation between positive contributions due to temperature and geopotential height changes and a negative contribution from humidity changes. Again, the contribution from changes in humidity is dominated by changes in saturation specific humidity.

As the entrainment rate is increased, the increase in boundary GMS_WC with warming becomes weaker. This is mostly related to the Δh contribution becoming more negative, but it is partially compensated for by the $\Delta\hat{\omega}$ contribution becoming more positive. The more negative changes in Δh are as expected given that entrainment makes the atmosphere less stable and has a greater effect in the warmer climate than the control climate (Singh & O'Gorman, 2013). Looking at Figures 5c,f, since entrainment has more of an effect on $\hat{\omega}$ in the warmer climate, increasing the entrainment rate will also make the $\Delta\hat{\omega}$ contribution more positive. Thus increasing entrainment does dampen the increase in boundary GMS_WC with warming as was expected initially, but there is less of an effect than would occur if only changes in MSE were considered.

Figure 9 shows that changes in specific humidity are the main reason that the Δh contribution becomes more negative as the entrainment rate increase, while the contribution from changes in temperature does not vary noticeably across entrainment rates. Using the Clausius-Clapeyron relationship, the greater contribution from changes in specific humidity with increasing entrainment is consistent with temperature lapse rates steepening with increasing entrainment, and more so in a warmer climate (Held et al., 2007; Singh & O'Gorman, 2013). But why do changes in lapse rates with increasing entrainment not affect the temperature contribution? It appears to be because entrainment also affects the control-climate boundary GMS_WC and Figure 9 shows the fractional response to warming. If instead absolute changes in boundary GMS_WC with warming are considered (Figure S12), the temperature contribution does become less positive as the entrainment rate is increased as expected.

4 Conclusions

We have evaluated the response of the Walker circulation to warming in comprehensive and idealized GCM simulations using an energetic perspective, with an emphasis on the spread in the response across GCM projections. A surprising result of our study is that the spread across AMIP models, which all have the same imposed SST, is similar to the spread across CMIP6 models, which are coupled to a dynamic ocean. The spread of WC response in the AMIP models is 12% $\text{K}^{-1}$and the spread in CMIP6 models is 14% K^{-1}. Still, the strong role of the atmosphere does not preclude a role of the ocean since the spread from each component separately need not sum to the total spread of the coupled system. In addition, the ascent and descent regions of the WC are not in exactly

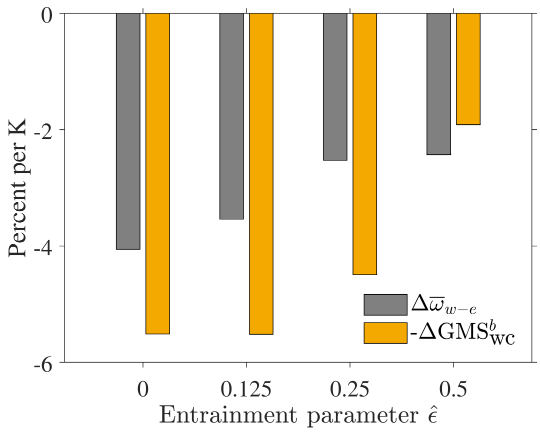

Figure 8. Response of WC strength (gray) to warming compared with minus the response of boundary $\mathrm{GMS_{WC}}$ (orange) in idealized GCM simulations with varying entrainment rates.

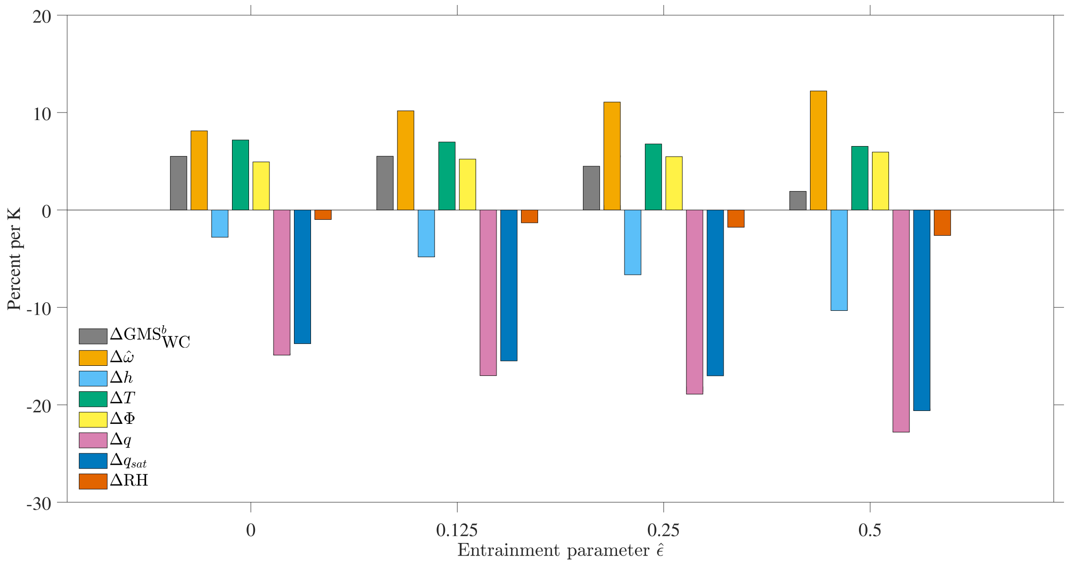

Figure 9. Same as Figure 6 but for idealized GCM simulations with varying entrainment rates and using the boundary $\mathrm{GMS_{WC}}$ instead of $\mathrm{GMS_{WC}}$.

the same location in each GCM which may complicate the comparison of CMIP6 simulations with the AMIP simulations in which the SST response is imposed the same way in all models. A potential candidate for the spread across AMIP models not considered here is the role of differences in resolution across models, given that WC strength is sensitive to resolution in an idealized atmospheric GCM (Silvers & Robinson, 2021).

In an MSE budget analysis of WC strength in CMIP6 and AMIP simulations, a weakening of the WC is related primarily to increases in $\mathrm{GMS_{WC}}$, and this weakening is amplified by changes in radiation. The gross moist stability thus emerges as a key factor, consistent with the heuristic idea that for a given energy transport, a higher GMS is associated with a weaker circulation. Changes in horizontal MSE advection and surface latent and sensible fluxes play a smaller role. We find a large spread in WC response to warming across CMIP6 and AMIP models, with $\mathrm{GMS_{WC}}$ response anticorrelated with WC response. The spread in $\mathrm{GMS_{WC}}$ response in AMIP models is 13% K^{-1}, and its spread in CMIP6 models is similar at 14% K^{-1}.

The role of radiation is substantial in both CMIP6 and AMIP models. In the CMIP6 models, there is a multimodel mean weakening of the WC of 12% K^{-1} with a multimodel mean contribution of 7% K^{-1} from radiation. In the AMIP models, there is a multimodel mean weakening of the WC of 12% K^{-1} with a multimodel mean contribution of 5% K^{-1} from radiation. The radiation contribution is always the same sign as the $\mathrm{GMS_{WC}}$ contribution; that is, contributing a weakening. Further, the decomposition of the radiation contribution (Figures 1c,d) indicates a strong role of WC-linked changes in radiation across CMIP6 and AMIP models. We find that cloud radiative feedbacks are amplifying the WC responses in CMIP6 and AMIP models, and such feedbacks have been previously found to affect the WC strength (e.g., Peters and Bretherton (2005)).

The $\mathrm{GMS_{WC}}$ response to warming involves changes in the vertical profiles of MSE and vertical velocity. Both the vertical profile of MSE and the shape of the vertical velocity profile contribute to the spread across CMIP6 and AMIP simulations in $\mathrm{GMS_{WC}}$ response. They are both sensitive to convective entrainment which is an uncertain and parameterized process in GCMs. Therefore, we evaluate the role of entrainment in setting $\mathrm{GMS_{WC}}$ and WC strength in an idealized GCM. To do so, we modify the simplified Betts Miller convection scheme of Frierson (2007) to include a simple representation of entrainment. We find that horizontal MSE advection plays an important role in the WC in some simulations, which is complicating because we do not have a theory for the relationship between entrainment and horizontal advection. To address this, we define a boundary $\mathrm{GMS_{WC}}$ which approximately includes the role of horizontal MSE advection while not involving horizontal velocities and horizontal MSE gradients. Rather, the boundary $\mathrm{GMS_{WC}}$ involves vertical advection of MSE profiles averaged over the boundary of each of the ascent and descent regions. We find that the WC weakens with warming, but less so at higher entrainment rates. This is consistent with increases in boundary $\mathrm{GMS_{WC}}$ that get weaker with increasing entrainment. The effect of increased entrainment on boundary $\mathrm{GMS_{WC}}$ response can be understood through the fact that entrainment tends to make the atmosphere less stable in terms of the vertical profile of MSE, and it does so to a greater extent in the warmer climate. However, entrainment also affects the shape of the vertical-velocity profile, and this tends to weaken the effect of entrainment on boundary $\mathrm{GMS_{WC}}$. The results from the idealized GCM provide a demonstration of a causal linkage between an imposed change in thermal stratification and resulting changes in WC strength in a way that is consistent with what would be expected from the energetic analysis.

We conclude that the atmosphere plays a key role in setting the spread in WC response to warming, especially through changes in $\mathrm{GMS_{WC}}$ and cloud-radiative feedbacks. Convective entrainment influences boundary $\mathrm{GMS_{WC}}$ response and thus the WC response in the idealized GCM. However, the spread in $\mathrm{GMS_{WC}}$ response across CMIP6 and AMIP models is primarily from intermodel differences in vertical velocity profiles and these intermodel differences are much bigger than the spread in vertical velocity profiles that results from changing entrainment in the idealized GCM. Thus it seems unlikely that differences in representation of entrainment are the dominant source of spread across CMIP6 and AMIP models. Rather, other influences on vertical velocity profiles are likely a major cause of the substantial spread in WC response in GCMs. The projected response of vertical velocity profiles to climate warming over the tropical oceans has been linked to changes in the horizontal pattern of boundary-layer temperature, including through their Laplacian (Lindzen & Nigam, 1987; Back & Bretherton, 2009; Duffy et al., 2020). There is no spread in the SST change in the AMIP simulations, but the Laplacian of boundary-layer temperature change is not fully determined by the SST change (Duffy et al., 2020). What determines the changes in the shape of the vertical velocity profiles in the East and West Pacific in particular should be investigated in future work.

Appendix A The entraining simplified Betts-Miller convection scheme

The SBM convection scheme of Frierson (2007) relaxes temperature profiles to a moist adiabat. Here, the scheme is modified such that temperature profiles are relaxed to a that of an *entraining* plume. The target humidity profile is calculated as in the original scheme using the target temperature profile (based on the entraining plume) and a reference relative humidity of 70%. The entrainment rate, ϵ, varies inversely with height and is given by $\epsilon = \frac{\hat{\epsilon}}{z}$, where $\hat{\epsilon}$ is a non-dimensional entrainment parameter and z is height. The convection scheme represents an ensemble of clouds, each of which detrains at a different level, which is crudely represented by the inverse relationship with z. The temperature lapse rate is assumed to be dry-adiabatic below the lifted condensation level (LCL). Above the LCL,

$$\frac{\partial h_s}{\partial z} = -\epsilon \left(h_s - h_e\right), \tag{A1}$$

where $h_s = c_pT + gz + Lr_s$ is the saturation MSE, r_s is the saturation mixing ratio, and h_e is the environmental MSE. Here we use the GCM's gridbox MSE to represent the environmental MSE. Using the definition of h_s gives

$$c_p\frac{dT}{dz} + g + L\frac{dr_s}{dz} = -\epsilon \left(h_s - h_e\right). \tag{A2}$$

Using $r_s = r_s(T, p)$ and applying the hydrostatic equation gives

$$c_p\frac{dT}{dz} + g + L\frac{\partial r_s}{\partial T}\frac{dT}{dz} - L\rho g\frac{\partial r_s}{\partial p} = -\epsilon \left(h_s - h_e\right). \tag{A3}$$

Next, group like terms to give

$$(c_p + L\frac{\partial r_s}{\partial T})\frac{\partial T}{\partial z} + g - L\rho g\frac{\partial r_s}{\partial p} = -\epsilon \left(h_s - h_e\right). \tag{A4}$$

Rearranging to solve for $\frac{\partial T}{\partial z}$ gives

$$\frac{\partial T}{\partial z} = \frac{-\epsilon \left(h_s - h_e\right) - g + L\rho g\frac{\partial r_s}{\partial p}}{c_p + L\frac{\partial r_s}{\partial T}}. \tag{A5}$$

Following the original scheme, we approximate the partial derivatives of r_s with respect to pressure and temperature as $\partial r_s/\partial p = -r_s/p$ and $\partial r_s/\partial T = Lr_s/(R_vT^2)$, respectively, where R_v is the gas constant for water vapor. Substituting these two expressions into Equation A5 and applying the ideal gas law gives

$$\frac{\partial T}{\partial z} = \frac{-\epsilon \left(h_s - h_e\right) - g(1 + \frac{Lr_s}{RT})}{c_p + \frac{L^2r_s}{R_vT^2}}. \tag{A6}$$

Using the hydrostatic equation and the ideal gas law gives the lapse rate of the entraining plume above the LCL

$$\frac{\partial T}{\partial \ln p} = \frac{\frac{RT}{gc_p}\epsilon \left(h_s - h_e\right) + \frac{RT}{c_p} + \frac{Lr_s}{c_p}}{1 + \frac{L^2r_s}{c_pR_vT^2}}. \tag{A7}$$

Notice that the temperature profile for the entraining plume reduces to a moist adiabat when $\epsilon = 0$.

Open Research

We acknowledge the World Climate Research Programme, which, through its Working Group on Coupled Modelling, coordinated and promoted CMIP6. We thank the climate modeling groups for producing and making available their model output, the Earth System Grid Federation (ESGF) for archiving the data and providing access, and the

multiple funding agencies who support CMIP6 and ESGF. Each model and the variant ID of the simulations used is listed in Table S1. The modified version of the GFDL idealized moist spectral atmospheric model and the analysis scripts used for this work are available on Zenodo at https://doi.org/10.5281/zenodo.6620842.

Acknowledgments

We thank Robert Jnglin Wills, Tristan Abbott, and Janni Yuval for help in setting up the idealized GCM simulations. We thank Larissa Back, Tim Cronin, and Adam Schlosser for useful feedback. We thank Robert Jnglin Wills and two anonymous reviewers for very thoughtful feedback which improved the paper. This research was supported by NSF-AGS 1749986. This research was completed in part at the National Center for Atmospheric Research, which is a major facility sponsored by the National Science Foundation under Cooperative Agreement No. 1852977. Computing resources were provided by the Climate Simulation Laboratory at NCAR's Computational and Information Systems Laboratory (CISL).

References

Back, L. E., & Bretherton, C. S. (2009). On the relationship between SST gradients, boundary layer winds, and convergence over the tropical oceans. *Journal of Climate*, *22*(15), 4182–4196. doi: 10.1175/2009JCLI2392.1

Bentsen, M., Olivië, D. J. L., Seland, o., Toniazzo, T., Gjermundsen, A., & et al. (2019). NCC NorESM2-MM model output prepared for CMIP6 CMIP historical and ScenarioMIP ssp585. Earth System Grid Federation. (Version: 20191108 [dataset]) doi: https://doi.org/10.22033/ESGF/CMIP6.506

Boucher, O., Denvil, S., Levavasseur, G., Cozic, A., Caubel, A., Foujols, M.-A., & et al. (2018). IPSL IPSL-CM6A-LR model output prepared for CMIP6 CMIP historical, ScenarioMIP ssp585, CMIP amip, and CFMIP amip-future4K. Earth System Grid Federation. (Version: 20180803 [dataset]) doi: https://doi.org/10.22033/ESGF/CMIP6.1521

Byun, Y.-H., Lim, Y.-J., Shim, S., Sung, H. M., Sun, M., Kim, J., & et al. (2019). NIMS-KMA KACE1.0-G model output prepared for CMIP6 CMIP historical ScenarioMIP ssp585. Earth System Grid Federation. (Version: 20190920 [dataset]) doi: https://doi.org/10.22033/ESGF/CMIP6.2241

Cao, J. (2019). NUIST NESMv3 model output prepared for CMIP6 CMIP historical and ScenarioMIP ssp585. Earth System Grid Federation. (Version: 20190728 [dataset]) doi: https://doi.org/10.22033/ESGF/CMIP6.2021

Chou, C., & Neelin, J. D. (2004). Mechanisms of global warming impacts on regional tropical precipitation. *Journal of Climate*, *17*(13), 2688–2701. doi: 10.1175/1520-0442(2004)017⟨2688:MOGWIO⟩2.0.CO;2

Chou, C., Wu, T.-C., & Tan, P.-H. (2013). Changes in gross moist stability in the tropics under global warming. *Climate Dynamics*, *41*(9-10), 2481–2496. doi: https://doi.org/10.1007/s00382-013-1703-2

Clement, A. C., Seager, R., Cane, M. A., & Zebiak, S. E. (1996). An ocean dynamical thermostat. *Journal of Climate*, *9*(9), 2190–2196. doi: https://doi.org/10.1175/1520-0442(1996)009⟨2190:AODT⟩2.0.CO;2

Cole, J. N., von Salzen, K., Swart, N. C., Kharin, V. V., Lazare, M., Scinocca, J. F., & et al. (2019). CCCma CanESM5 model output prepared for CMIP6 CFMIP amip-future4K. Earth System Grid Federation. (Version: 20190429 [dataset]) doi: https://doi.org/10.22033/ESGF/CMIP6.1301

Consortium, E.-E. (2019). EC-Earth-Consortium EC-Earth3 model output prepared for CMIP6 CMIP historical and ScenarioMIP ssp585. Earth System Grid Federation. (Version: 20200310 [dataset]) doi: https://doi.org/10.22033/ESGF/CMIP6.181

Danabasoglu, G. (2019). NCAR CESM2 model output prepared for CMIP6 CMIP historical, ScenarioMIP ssp585, CMIP amip, and CFMIP amip-future4K. Earth System Grid Federation. (Version: 20190401 [dataset]) doi: https://doi.org/10.22033/ESGF/CMIP6.2181

DiNezio, P. N., Clement, A. C., Vecchi, G. A., Soden, B. J., & Kirtman, B. P. (2009). Climate response of the equatorial pacific to global warming. *Journal of Climate*, *22*(18), 4873–4892. doi: https://doi.org/10.1175/2009JCLI2982.1

Dix, M., Bi, D., Dobrohotoff, P., Fiedler, R., Harman, I., Law, R., & et al. (2019). CSIRO-ARCCSS ACCESS-CM2 model output prepared for CMIP6 CMIP historical and ScenarioMIP ssp585. Earth System Grid Federation. (Version: 20210317 [dataset]) doi: https://doi.org/10.22033/ESGF/CMIP6.2281

Duffy, M. L., O'Gorman, P. A., & Back, L. E. (2020). Importance of Laplacian of low-level warming for the response of precipitation to climate change over Tropical oceans. *Journal of Climate*, *33*(10), 4403–4417. doi: 10.1175/JCLI-D-19-0365.1

Frierson, D. M. W. (2007). The dynamics of idealized convection schemes and their effect on the zonally averaged Tropical circulation. *Journal of the Atmospheric Sciences*, *64*(6), 1959–1976. doi: https://doi.org/10.1175/JAS3935.1

Frierson, D. M. W., Held, I. M., & Zurita-Gotor, P. (2006). A gray-radiation aquaplanet moist GCM. Part I: Static stability and eddy scale. *Journal of the Atmospheric Sciences*, *63*(10), 2548–2566. doi: https://doi.org/10.1175/JAS3753.1

Good, P. (2020). MOHC HadGEM3-GC31-LL model output prepared for CMIP6 ScenarioMIP ssp585. Earth System Grid Federation. (Version: 20200114 [dataset]) doi: https://doi.org/10.22033/ESGF/CMIP6.10845

Hartmann, D. L. (2022). The Antarctic ozone hole and the pattern effect on climate sensitivity. *Proceedings of the National Academy of Sciences*, *119*(35), e2207889119. doi: 10.1073/pnas.2207889119

Heede, U. K., & Fedorov, A. V. (2021). Eastern equatorial Pacific warming delayed by aerosols and thermostat response to CO2 increase. *Nature Climate Change*, *11*(8), 696–703. doi: https://doi.org/10.1038/s41558-021-01101-x

Held, I. M., & Soden, B. J. (2006). Robust responses of the hydrological cycle to global warming. *Journal of Climate*, *19*(21), 5686–5699. doi: https://doi.org/10.1175/JCLI3990.1

Held, I. M., Zhao, M., & Wyman, B. (2007). Dynamic radiative-convective equilibria using GCM column physics. *Journal of the Atmospheric Sciences*, *64*(1), 228–238. doi: https://doi.org/10.1175/JAS3825.11

Inoue, K., Biasutti, M., & Fridlind, A. M. (2021). Evidence that horizontal moisture advection regulates the ubiquitous amplification of rainfall variability over Tropical oceans. *Journal of the Atmospheric Sciences*, *78*(2), 529–547. doi: https://doi.org/10.1175/JAS-D-20-0201.1

John, J. G., Blanton, C., McHugh, C., Radhakrishnan, A., Rand, K., Vahlenkamp, H., & et al. (2018). NOAA-GFDL GFDL-ESM4 model output prepared for CMIP6 ScenarioMIP ssp585. Earth System Grid Federation. (Version: 20180701 [dataset]) doi: https://doi.org/10.22033/ESGF/CMIP6.1407

Kang, S. M., Xie, S.-P., Shin, Y., Kim, H., Hwang, Y.-T., Stuecker, M. F., ... Hawcroft, M. (2020). Walker circulation response to extratropical radiative forcing. *Science Advances*, *6*(47), eabd3021. doi: 10.1126/sciadv.abd3021

Keil, P., Schmidt, H., Stevens, B., & Bao, J. (2021). Variations of tropical lapse rates in climate models and their implications for upper tropospheric warming. *Journal of Climate*, 1–50. doi: https://doi.org/10.1175/JCLI-D-21-0196.1

Knutson, T. R., & Manabe, S. (1995). Time-mean response over the Tropical Pacific to increased CO_2 in a coupled ocean-atmosphere model. *Journal of Climate*, *8*(9), 2181–2199. doi: https://doi.org/10.1175/1520-0442(1995)008⟨2181:TMROTT⟩2.0.CO;2

Krasting, J. P., John, J. G., Blanton, C., McHugh, C., Nikonov, S., Radhakrishnan, A., & et al. (2018). NOAA-GFDL GFDL-ESM4 model output prepared for CMIP6 CMIP historical. Earth System Grid Federation. (Version: 20190726 [dataset]) doi: https://doi.org/10.22033/ESGF/CMIP6.1407

Lee, W.-L., & Liang, H.-C. (2019). AS-RCEC TaiESM1.0 model output prepared for CMIP6 CMIP historical, CMIP, ScenarioMIP ssp585, and CMIP amip. Earth System Grid Federation. (Version: 20200817 [dataset]) doi: https://doi.org/10.22033/ESGF/CMIP6.9684

L'Heureux, M. L., Lee, S., & Lyon, B. (2013). Recent multidecadal strengthening of the Walker circulation across the tropical Pacific. *Nature Climate Change*, *3*(6), 571–576. doi: 10.1038/nclimate1840

Lindzen, R. S., & Nigam, S. (1987). On the role of sea surface temperature gradients in forcing low-level winds and convergence in the tropics. *Journal of the Atmospheric Sciences*, *44*(17), 2418–2436. doi: 10.1175/1520-0469(1987)044⟨2418:OTROSS⟩2.0.CO;2

Lovato, T., & Peano, D. (2020). CMCC CMCC-CM2-SR5 model output prepared for CMIP6 CMIP historical and ScenarioMIP ssp585. Earth System Grid Federation. (Version: 20200622 [dataset]) doi: https://doi.org/10.22033/ESGF/CMIP6.1362

Ma, J., Xie, S.-P., & Kosaka, Y. (2012). Mechanisms for tropical tropospheric circulation change in response to global warming. *Journal of Climate*, *25*(8), 2979–2994. doi: https://doi.org/10.1175/JCLI-D-11-00048.1

Merlis, T. M. (2015). Direct weakening of tropical circulations from masked CO_2 radiative forcing. *Proceedings of the National Academy of Sciences*, *112*(43), 13167–13171. doi: https://doi.org/10.1073/pnas.1508268112

Merlis, T. M., & Schneider, T. (2011). Changes in zonal surface temperature gradients and Walker circulations in a wide range of climates. *Journal of Climate*, *24*(17), 4757–4768. doi: https://doi.org/10.1175/2011JCLI4042.1

Merlis, T. M., Schneider, T., Bordoni, S., & Eisenman, I. (2013). Hadley circulation response to orbital precession. Part II: Subtropical continent. *Journal of Climate*, *26*(3), 754–771. doi: https://doi.org/10.1175/JCLI-D-12-00149.1

Miyawaki, O., Tan, Z., Shaw, T. A., & Jansen, M. F. (2020). Quantifying key mechanisms that contribute to the deviation of the tropical warming profile from a moist adiabat. *Geophysical Research Letters*, *47*(20). doi: https://doi.org/10.1029/2020GL089136

Neelin, J. D., & Held, I. M. (1987). Modeling tropical convergence based on the moist static energy budget. *Monthly Weather Review*, *115*(1), 3–12. doi: https://doi.org/10.1175/1520-0493(1987)115⟨0003:MTCBOT⟩2.0.CO;2

O'Gorman, P. A., & Schneider, T. (2008). The hydrological cycle over a wide range of climates simulated with an idealized GCM. *Journal of Climate*, *21*(15), 3815–3832. doi: https://doi.org/10.1175/2007JCLI2065.1

Ogura, T., Watanabe, M., & Hirota, N. (2019). MIROC MIROC6 model output prepared for CMIP6 CFMIP amip-future4K. Earth System Grid Federation. (Version: 20190705 [dataset]) doi: https://doi.org/10.22033/ESGF/CMIP6.885

Peters, M. E., & Bretherton, C. S. (2005). A simplified model of the Walker circulation with an interactive ocean mixed layer and cloud-radiative feedbacks. *Journal of Climate*, *18*(20), 4216–4234. doi: 10.1175/JCLI3534.1

Raymond, D. J., Sessions, S. L., Sobel, A. H., & Fuchs, Z. (2009). The mechanics of gross moist stability. *Journal of Advances in Modeling Earth Systems*, *1*(3). doi: https://doi.org/10.3894/JAMES.2009.1.9

Ridley, J., Menary, M., Kuhlbrodt, T., Andrews, M., & Andrews, T. (2019). MOHC HadGEM3-GC31-LL model output prepared for CMIP6 CMIP amip. Earth System Grid Federation. (Version: 20191001 [dataset]) doi: https://doi.org/10.22033/ESGF/CMIP6.419

Romps, D. M. (2010). A direct measure of entrainment. *Journal of the Atmospheric*

Sciences, *67*(6), 1908–1927. doi: https://doi.org/10.1175/2010JAS3371.1

Semmler, T., Danilov, S., Rackow, T., Sidorenko, D., Barbi, D., Hegewald, J., & et al. (2019). AWI AWI-CM1.1MR model output prepared for CMIP6 CMIP historical and ScenarioMIP ssp585. Earth System Grid Federation. (Version: 20190529 [dataset]) doi: https://doi.org/10.22033/ESGF/CMIP6.359

Shiogama, H., Abe, M., & Tatebe, H. (2019). MIROC MIROC6 model output prepared for CMIP6 ScenarioMIP ssp585. Earth System Grid Federation. (Version: 20190627 [dataset]) doi: https://doi.org/10.22033/ESGF/CMIP6.898

Shiu, C.-J., Lee, W.-L., & Hsu, H.-H. (2021). AS-RCEC TaiESM1.0 model output prepared for CMIP6 CFMIP amip-future4K. Earth System Grid Federation. (Version: 20210820 [dataset]) doi: https://doi.org/10.22033/ESGF/CMIP6.9683

Silvers, L. G., & Robinson, T. (2021). Clouds and radiation in a mock Walker circulation. *Journal of Advances in Modeling Earth Systems*, *13*(2). doi: 10.1029/2020MS002196

Singh, M. S., & Neogi, S. (2022). On the interaction between moist convection and large-scale ascent in the tropics. *Journal of Climate*, *35*(14), 4417–4435. doi: https://doi.org/10.1175/JCLI-D-21-0717.1

Singh, M. S., & O'Gorman, P. A. (2012). Upward shift of the atmospheric general circulation under global warming: Theory and simulations. *Journal of Climate*, *25*(23), 8259–8276. doi: https://doi.org/10.1175/JCLI-D-11-00699.1

Singh, M. S., & O'Gorman, P. A. (2013). Influence of entrainment on the thermal stratification in simulations of radiative-convective equilibrium. *Geophysical Research Letters*, *40*(16), 4398–4403. doi: https://doi.org/10.1002/grl.50796

Sohn, B.-J., Lee, S., Chung, E.-S., & Song, H.-J. (2016). The role of the dry static stability for the recent change in the Pacific Walker circulation. *Journal of Climate*, *29*(8), 2765–2779. doi: https://doi.org/10.1175/JCLI-D-15-0374.1

Song, Z., Qiao, F., Bao, Y., Shu, Q., Song, Y., & Yang, X. (2019). FIO-QLNM FIO-ESM2.0 model output prepared for CMIP6 CMIP historical and ScenarioMIP ssp585. Earth System Grid Federation. (Version: 20191226 [dataset]) doi: https://doi.org/10.22033/ESGF/CMIP6.9047

Swart, N. C., Cole, J. N., Kharin, V. V., Lazare, M., Scinocca, J. F., Gillett, N. P., & et al. (2019). CCCma CanESM5 model output prepared for CMIP6 CMIP historical, ScenarioMIP ssp585, and CMIP amip. Earth System Grid Federation. (Version: 20190429 [dataset]) doi: https://doi.org/10.22033/ESGF/CMIP6.10205

Tan, Z., Lachmy, O., & Shaw, T. A. (2019). The sensitivity of the jet stream response to climate change to radiative assumptions. *Journal of Advances in Modeling Earth Systems*, *11*(4), 934–956. doi: 10.1029/2018MS001492

Tatebe, H., & Watanabe, M. (2018). MIROC MIROC6 model output prepared for CMIP6 CMIP historical and CMIP amip. Earth System Grid Federation. (Version: 20181212 [dataset]) doi: https://doi.org/10.22033/ESGF/CMIP6.881

Tokinaga, H., Xie, S.-P., Deser, C., Kosaka, Y., & Okumura, Y. M. (2012). Slowdown of the Walker circulation driven by tropical Indo-Pacific warming. *Nature*, *491*(7424), 439–443. doi: 10.1038/nature11576

Trenberth, K. E., & Stepaniak, D. P. (2003). Seamless poleward atmospheric energy transports and implications for the Hadley circulation. *Journal of Climate*, *16*(22), 3706–3722. doi: https://doi.org/10.1175/1520-0442(2003)016⟨3706:SPAETA⟩2.0.CO;2

Vecchi, G. A., & Soden, B. J. (2007). Global warming and the weakening of the tropical circulation. *Journal of Climate*, *20*(17), 4316–4340. doi: https://doi.org/10.1175/JCLI4258.1

Vecchi, G. A., Soden, B. J., Wittenberg, A. T., Held, I. M., Leetmaa, A., & Harrison, M. J. (2006). Weakening of tropical Pacific atmospheric circulation due to anthropogenic forcing. *Nature*, *441*(7089), 73–76. doi:

https://doi.org/10.1038/nature04744

Voldoire, A. (2018). CNRM-CERFACS CNRM-CM6-1 model output prepared for CMIP6 CMIP historical, ScenarioMIP ssp585, CMIP amip and CFMIP amip-future4K. Earth System Grid Federation. (Version: 20181203 [dataset]) doi: https://doi.org/10.22033/ESGF/CMIP6.1374

Volodin, E., Mortikov, E., Gritsun, A., Lykossov, V., Galin, V., Diansky, N., & et al. (2019). INM INM-CM5-0 model output prepared for CMIP6 CMIP historical and ScenarioMIP ssp585. Earth System Grid Federation. (Version: 20190610 [dataset]) doi: https://doi.org/10.22033/ESGF/CMIP6.1423

Webb, M. (2019). MOHC HadGEM3-GC31-LL model output prepared for CMIP6 CMIP historical and CFMIP amip-future4K. Earth System Grid Federation. (Version: 20191216 [dataset]) doi: https://doi.org/10.22033/ESGF/CMIP6.435

Wieners, K.-H., Giorgetta, M., Jungclaus, J., Reick, C., Esch, M., Bittner, M., & et al. (2019). MPI-M MPI-ESM1.2-LR model output prepared for CMIP6 CMIP historical and ScenarioMIP ssp585. Earth System Grid Federation. (Version: 20190710 [dataset]) doi: 10.22033/ESGF/CMIP6.6705

Wills, R. C. J., Dong, Y., Proistosecu, C., Armour, K. C., & Battisti, D. S. (2022). Systematic climate model biases in the large-scale patterns of recent sea surface temperature and sea-level pressure change. *Geophysical Research Letters*, *49*(17). doi: 10.1029/2022GL100011

Wills, R. C. J., Levine, X. J., & Schneider, T. (2017). Local energetic constraints on Walker circulation strength. *Journal of the Atmospheric Sciences*, *74*(6), 1907–1922. doi: https://doi.org/10.1175/JAS-D-16-0219.1

Wu, T., Chu, M., Dong, M., Fang, Y., Jie, W., Li, J., & et al. (2019). BCC BCC-CSM2MR model output prepared for CMIP6 CMIP historical, CMIP amip and CFMIP amip-future4K. Earth System Grid Federation. (Version: 20200720 [dataset]) doi: https://doi.org/10.22033/ESGF/CMIP6.2856

Xin, X., Wu, T., Shi, X., Zhang, F., Li, J., Chu, M., & et al. (2019). BCC BCC-CSM2MR model output prepared for CMIP6 ScenarioMIP ssp585. Earth System Grid Federation. (Version: 20190314 [dataset]) doi: https://doi.org/10.22033/ESGF/CMIP6.1725

Yu, Y. (2019). CAS FGOALS-f3-L model output prepared for CMIP6 CMIP historical and ScenarioMIP ssp585. Earth System Grid Federation. (Version: 20191013 [dataset]) doi: https://doi.org/10.22033/ESGF/CMIP6.1782

Yukimoto, S., Koshiro, T., Kawai, H., Oshima, N., Yoshida, K., Urakawa, S., & et al. (2019). MRI MRI-ESM2.0 model output prepared for CMIP6 CMIP historical, ScenarioMIP ssp585, CMIP amip, and CFMIP amip-future4K. Earth System Grid Federation. (Version: 20190625 [dataset]) doi: https://doi.org/10.22033/ESGF/CMIP6.623